Macroscopic excitation energy transport in a structured Co nanolayer

Igor Khmelinskii[1] and Vladimir I. Makarov[2,*]
[1]*University of the Algarve, FCT, DQF, 8005–139, Faro, Portugal*
[2]*University of Puerto Rico, Rio Piedras Campus, P.O. Box 23343, San Juan, Puerto Rico 00931-3343, USA*
(Received 4 July 2017; revised manuscript received 17 October 2017; published 3 November 2017)

We report absorption spectra of the 7.3- and 11.3-nm Co nanolayers and emission of a structured Co nanolayer. The structure contains a 7.3-nm Co nanolayer covering a $25 \times 25\,\mathrm{mm}^2$ fused silica substrate, with a thicker 11.3-nm Co track in the middle of the substrate. We report that the radiation energy absorbed by the entire Co nanolayer is transferred to the thicker nanotrack. The transferred energy is reemitted by the track, with the emission spectra containing well-defined emission bands, strongly dependent on the excitation wavelength. We report that the bands appearing in the emission spectra of the nanotrack correspond to the transitions from the higher electronic excited states of the nanotrack to its first excited state. We therefore identify the observed emission as the superemission of the Co nanotrack. The superemission quantum yield is dependent on the excitation wavelength, decreasing at higher excitation energies. We propose a theoretical model that explains the results obtained. The model analysis produced estimates of several model parameters.

DOI: 10.1103/PhysRevB.96.195405

I. INTRODUCTION

Many interesting physical phenomena are observed in nanoscaled systems [1–13]. Among these, plasmon generation in nanostructures was studied quite extensively [1–4]. The electromagnetic field radiation could be focused to nanoscale spot size using nanocapillaries and nanofibers covered by a highly conductive material, typically gold [1–4]. Oulton *et al.* (2008) [14] proposed a new approach that integrates dielectric waveguiding with plasmonics. They [14] defined a hybrid optical waveguide as a device that consists of a dielectric nanowire separated from a metal surface by a nanoscale dielectric gap. It was noted [15] that coupling between the plasmonic and waveguide modes across the gap enables "capacitorlike" energy storage that allows effective subwavelength transmission in nonmetallic regions. They also [14] demonstrated that in this case surface plasmons can travel over 40–150 μm with a strong mode confinement. Maier *et al.* (2003) [15] studied electromagnetic energy transfer from a localized subwavelength source to a localized detector, over distances of ca. 0.5 μm in plasmon waveguides, built of closely spaced silver rods. The waveguides were excited by the tip of a near-field scanning optical microscope, and the energy transport was probed by fluorescent nanospheres. These studies [14,15] are directly related to the data than we reported earlier [5–13], with quantum confinement always observable. We also reported exchange-resonance spectra for three-nanolayer sandwich structures, with nanolayers of different physical and chemical nature, and spin-polarized state transport in the same structures. Interesting results were obtained in a single-atomic-layer graphene (SLG) film [16] due to the p-wave triggered superconductivity in the graphene layer on an electron-doped oxide superconductor. Electron pairing in a vast majority of superconductors follows the Bardeen-Cooper-Schrieffer theory of superconductivity, which describes the condensation of electrons into pairs with antiparallel spins into a singlet state with an s-wave symmetry. Unconventional superconductivity was predicted in SLG, with the electrons pairing with a p-wave or chiral d-wave symmetry, depending on the position of the Fermi energy with respect to the Dirac point. By placing SLG on an electron-doped (nonchiral) d-wave superconductor and performing local scanning tunneling microscopy and spectroscopy, the authors obtained evidence for a p-wave triggered superconducting density of states in SLG. These results offer an exciting route for the development of p-wave superconductivity using two-dimensional materials with transition temperatures above 4.2 K [16].

Earlier we reported superemission in metal nanolayers and vertically aligned carbon nanotubes [17,18]. We also reported absorption, emission, and superemission in Cr nanolayers [17], providing experimental estimates of the energy density and power density of superemission of Cr nanolayers, along with the estimates of the diffraction-limited light divergence. We reported that the divergence of the superemission normal to the nanolayer corresponds to that of a point source, with the divergence angle of ca. 0.2 rad. We also reported surprising long-range transfer of the excitation energy in Cr metal films, at macroscopic distances of 1 cm. We additionally reported superemission of vertically aligned carbon nanotubes [18] in two samples sized $0.02 \times 0.2 \times 1.0\,\mathrm{cm}^3$ and $0.2 \times 0.2 \times 1.0\,\mathrm{cm}^3$. Both absorption and emission of nanotubes were strongly anisotropic. We found [17] that the emission spectra of such nanotubes extend from the mid-infrared range to the near-infrared range. Optical pumping of nanotube bundles in the direction normal to their axis produced superemission directed along their axis. The superemission band peaked at $7206 \pm 0.4\,\mathrm{cm}^{-1}$. We estimated the superemission energy and power density, along with diffraction-limited beam divergence. We found [17] that at the pumping energy of 3 mJ/pulse, the total superemission energy achieved 1.48 mJ/pulse, with the energy density of $18.5\,\mathrm{mJ\,cm}^{-2}$/pulse and power density of $1.2 \times 10^5\,\mathrm{W\,cm}^{-2}$/pulse. We also developed a detailed theory, describing with an acceptable accuracy all of the results obtained [17,18].

Presently we report excitation energy transport to a linear Co nanotrack 11.3 nm thick and 0.1 mm wide in the middle of the 7.3-nm Co nanolayer deposited on a $25 \times 25\,\mathrm{mm}^2$

*Corresponding author: vmvimakarov@gmail.com

fused silica substrate. The nanotrack is thus 4 nm higher than the nanolayer and 25 mm long. According to our earlier results [19,20], the electronic state density in the nanotrack system should be larger than that in the nanolayer, with lower-lying excited states that may accept the excitation energy. Thus, we can expect that the nanotrack will receive the light energy absorbed by the entire sample surface, reemitting it primarily along its length, similarly to what we observed with superemission of a laser-excited Cr nanolayer. Indeed, we detected directional energy transport towards the nanotrack. We measured the energy-transfer efficiency, the nanotrack emission spectrum, and the beam divergence at different excitation wavelengths. The results obtained may be used to build efficient solar energy concentrators based on nanolayers.

II. EXPERIMENTAL METHODS

A. Sample preparation

A square fused silica substrate (Shin-Etsu Quartz Products Co., $25 \times 25 \times 3\,\text{mm}^3$) was cleaned for 20 min by sonication in 30 ml of isopropanol with 25 mg commercial diamond powder (Diamond Technology, Inc.). Next the substrate was washed in pure isopropanol and deionized water. A commercial Co target (Diamond Technology, Inc.) was used to deposit nanocrystalline films on a commercial sputtering/thermo-evaporation Benchtop Turbo deposition system (Denton Vacuum). The substrate temperature was 475 °C. After deposition the samples were annealed at 600 °C in N_2 at 1 atm for 2 hours. We performed annealing to reduce the concentration of defects in the nanolayers. The film thickness was controlled by x-ray diffraction (XRD) (11) on an X'Pert materials research diffraction (MRD) system (PANalytic) calibrated with standard nanofilms of the same material. The estimated absolute uncertainty of film thickness was 2.5%; the relative uncertainties were much smaller, determined by the shutter opening times of the deposition system. The Co nanotrack was created using a variable-width slit. Figure 1 shows the diagram of the structured nanolayer sample.

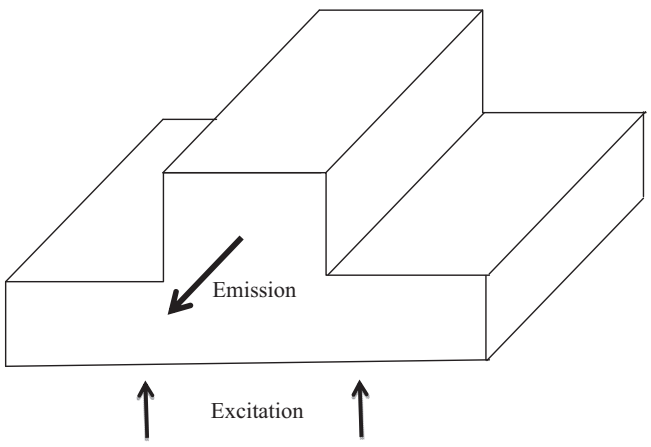

FIG. 1. Design of the structured Co nanolayer.

B. Measurement methods

The absorption spectra were recorded on Hitachi U-3900H UV-visible and Shimadzu UV-3600 Plus spectrophotometers. The spectral peak maxima and widths were calculated using PEAKFIT software (Sigmaplot). The samples were reproducibly installed into a support of blackened aluminum.

The emission spectra were measured using a high-pressure 200–500-W Xe-Hg lamp (Research Arc Lamp Sources, Newport, Inc.). The radiation was collected by appropriate lenses, filtered by a water-cooled glass filter to separate the individual emission bands, and defocused onto the entire sample surface. The UV-VIS emission was collected by a CaF_2 lens onto the entrance slit of the monochromator (Cornerstone 130 1/8 m Monochromator, Newport, Inc.), and detected by a photodiode (PD1; DET10A Si biased detector, Thorlabs). The output of the PD1 signal was digitized by a PCI-6034E DAQ I/O board (National Instruments), with the control code in the LABVIEW environment running on a Dell PC. The near-infrared and middle-infrared emission was focused onto the input slit of a FTIR spectrometer, the spectra were scanned, and the data collected by a PC computer.

Time-resolved emission experiments were carried using the fundamental harmonic and frequency-doubled (beta barium borate crystal) radiation of a dye laser (LPD-2000, Λ-Physics, with Coumarin-4 dye, 370–580-nm range; frequency-doubled radiation at 220–290 nm), pumped by the fourth harmonic (266.8 nm) of a YAG laser (Surelight-II, Continuum, Inc.). The laser pulse duration was about 7–10 ns. The dye laser radiation was defocused onto the entire sample surface. The emission was collected by a 30-cm spherical CaF_2 lens and registered by a photodiode (PD1; DET10A biased Si detector from Thorlabs) after passing through a neutral density filter. The data acquisition system was controlled by a PC computer using a digital oscilloscope (WaveSurfer 400, LeCroy). The detected emission was selected by an appropriate interference filter. The presently developed experimental methods allowed recording the time evolution of the emission with 2.5 ns resolution. All of the experiments were carried out at 77 K, unless expressly specified otherwise.

III. RESULTS AND DISCUSSION

A. Absorption spectra

Absorption spectra of separate Co nanolayers with 7.3 and 11.3 nm thickness deposited on fused silica substrates are shown in Fig. 2. The recorded spectra are in agreement with the data reported earlier [19]; however, some difference should be noted in the band intensity distribution and small band position shifts, as compared to the spectra reported earlier [18]. These differences may apparently be caused by differences in the sample preparation procedure, as the earlier reported samples were not annealed [19], contrary to the samples used in the present study. Note that we have not attempted to explore the effect of the annealing upon the absorption spectra; however, we assume that as a result the nanolayer will acquire a structure with a lower concentration of defects. This should have some effect on the spectra, at least, due to increased film density and smaller film thickness. We found that the spectral maxima are

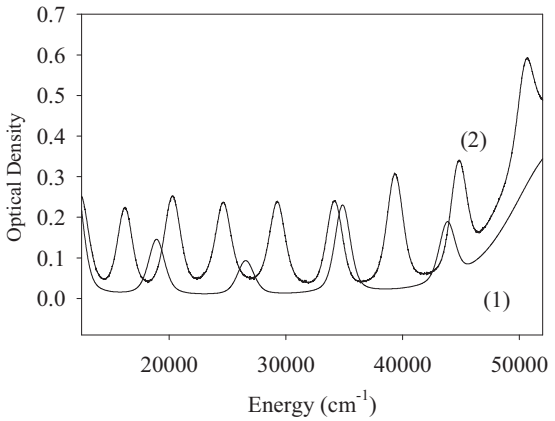

FIG. 2. Absorption spectra of Co nanolayers deposited on fused silica substrates: (1) 7.3 nm layer thickness, and (2) 11.3 nm layer thickness.

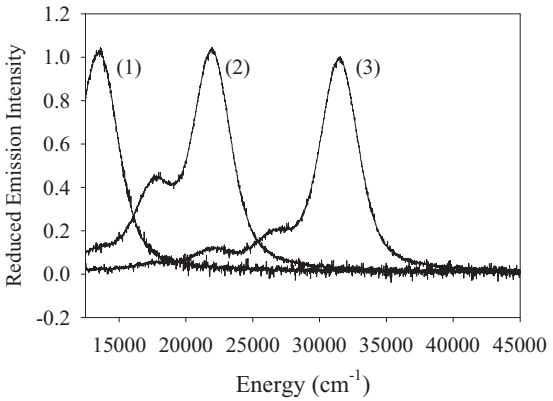

FIG. 3. Emission spectra of the track with the sample excited at: (1) 528.5 nm, (2) 376.5 nm, and (3) 286.9 nm, respectively.

well described by the relation

$$\Delta E_{mn} = 3029.2\frac{1}{fa^2}[2mn + m^2],\ \mathrm{cm}^{-1}. \qquad (1)$$

Here, for the Co nanolayers, $f = 0.1712$, $n = 8$ or 9, a is the nanolayer thickness in nanometers, and m is the quantum number change in the electronic $n \rightarrow n + m$ transition. To obtain the correct transition energies for the band maxima, we used $n = 8$ for $a = 7.3$ nm, and $n = 9$ for $a = 11.3$ nm.

B. Emission spectra

Taking into account the spectra of Fig. 2, we studied the emission properties of the sample assembly shown in Fig. 1. The sample was excited by an external radiation source, with the excitation beam normal to the sample surface. As we already noted, the beam was defocused, so that the entire sample surface was excited homogeneously. We recorded the emission spectra for the excitation radiation with wavelengths of 528.5, 376.5, and 286.9 nm, respectively, separated from the emission spectrum of the Xe-Hg lamp by appropriate interference filters (Optical Filters, Inc.). We report that in all cases the strongest emitting zones were located at the two extremities of the Co track (see Fig. 1), with Fig. 3 showing the respective emission spectra.

The emission spectra were fitted by a superposition of several bands, each described by a combination of Gaussian and Lorentzian functions:

$$I_{em}(\omega) = \sum_i \left[A_G e^{-\left(\frac{\omega_i-\omega}{\Omega_G}\right)^2} + \frac{A_L}{1+\left(\frac{\omega_i-\omega}{\Omega_L}\right)^2} \right], \qquad (2)$$

where $A_{G,i}, A_{L,i}, \Omega_{G,i}, \Omega_{L,i}, \omega_i$ are the fitting parameters describing each of the two functions, respectively, and i is the band number. We fitted the emission spectra using a commercial PEAKFIT software package. The resulting values of the fitting parameters are presented in Table I.

Optical transitions that correspond to the bands appearing in the emission spectra of the 11.3-nm-thick Co nanotrack are described by the quantum numbers shown in Table I. The higher n' excited electronic states of the Co nanotrack are populated by energy transfer from the excited states of the 7.3-nm Co nanolayer. Thus, the Co nanotrack is an energy acceptor, while the thinner 7.3-nm Co nanolayer is an energy donor. Since no transitions to the $n = 9$ are observable in the emission spectra, we interpret the emission as the superemission of the Co track. Note that only those bands appear in the emission of the 11.3-nm layer that have their energy below E_{exc} of 2384 cm^{-1}, the latter value being the energy difference between levels 9 and 10 in the 11.3-nm film (compare Tables I and III). Earlier we reported superemission (SE) from a homogeneous metal nanolayer that was excited directly [13], while here the nanotrack receives excitation via energy transfer. We measured both the excitation pulse energy reaching the sample surface and the SE pulse energy. The ratio of SE energy to the excitation energy equals 0.73 (1), 0.58 (2), and 0.39 (3), respectively, for the respective excitation wavelengths of Fig. 3. This ratio is the SE yield. We describe the model used to interpret these results below.

C. Time-resolved emission

Time-resolved experiments were carried out using the same excitation wavelengths of Fig. 3, with the relevant emission band isolated using an appropriate interference filter: (1) 740 nm, (2) 570 nm, and (3) 320 nm. Typical emission kinetics are shown in Fig. 4.

The kinetics of Fig. 4(b) may be fitted by a double-exponential function

$$I_{em} = C(e^{-k_2 t} - e^{-k_1 t}), \qquad (3)$$

where k_1 and k_2 are the rate constants of the emission growth and decay, respectively, and C is the relative intensity. The values of the fitting parameters are listed in Table II.

We shall analyze the k_1 rate constant, describing the energy transfer as defined by the following system of equations, with CoI corresponding to the thin 7.3-nm layer and CoII to the thicker 11.3-nm track:

1. $\mathrm{CoI}^* + \mathrm{CoII} \rightarrow \mathrm{CoI} + \mathrm{CoII}^*$; k'_1
2. $\mathrm{CoI} + h\nu \rightarrow \mathrm{CoI}^*$;
3. $\mathrm{CoI}^* \rightarrow \mathrm{CoI} + h\nu_{em}$; $1/\tau_{1,em}$
4. $\mathrm{CoI}^* \rightarrow \mathrm{CoI}$; $k_{1,nr}$
5. $\mathrm{CoII}^* \rightarrow \mathrm{CoII} + h\nu_{em}$; $1/\tau_{2,em}$
6. $\mathrm{CoII}^* \rightarrow \mathrm{CoII}$; $k_{2,nr}$

TABLE I. Values of the spectral fitting parameters $A_{G,i}$, $A_{L,i}$, $\Omega_{G,i}$, $\Omega_{L,i}$, and ω_i for the emission spectra and the quantum numbers for the emission bands of Fig. 3.

Excitation wavelength	Spectrum number of Fig. 3	Initial state quantum number n'	Final state quantum number n	$A_{G,i}$	$A_{L,i}$	$\Omega_{G,i}(\mathrm{cm}^{-1})$	$\Omega_{L,i}(\mathrm{cm}^{-1})$	$\omega_i(\mathrm{cm}^{-1})$
528.5 nm 18921 cm^{-1}	1	14	10	0.55	0.45	1967	1893	13522
376.5 nm/ 26560 cm^{-1}	2	14	10	0.028	0.024	1879	1975	13521
	2	15	10	0.171	0.069	1907	1903	17596
	2	16	10	0.346	0.359	1762	1892	21946
	3	14	10	0.0027	0.0023	1897	1895	13523
286.9 nm/ 34855 cm^{-1}	3	15	10	0.0167	0.0067	1934	1842	17591
	3	16	10	0.0338	0.0351	1903	1769	21944
	3	17	10	0.0517	0.0543	1801	1879	26573
	3	18	10	0.4237	0.3730	1923	1905	31478

where $\tau_{1,em}$, $\tau_{2,em}$ are the emission lifetimes of the CoI* and CoII* layers, and $k_{1,nr}$ and $k_{2,nr}$ are the rate constants of the radiationless processes in CoI* and CoII*. The resulting excited-state dynamics is described by the following system of differential equations:

$$\begin{aligned}\frac{dn_{\mathrm{CoI}^*}}{dt} &= -\left(\frac{1}{\tau_{1,em}} + k_{1,nr} + k'_1\right)n_{\mathrm{CoI}^*},\\ \frac{dn_{\mathrm{CoII}^*}}{dt} &= k'_1 n_{\mathrm{CoI}^*} - \left(\frac{1}{\tau_{2,em}} + k_{2,nr}\right)n_{\mathrm{CoII}^*}.\end{aligned} \tag{4}$$

The solution of this system is given by

$$\begin{aligned}n_{\mathrm{CoI}^*}(t) &= n_{\mathrm{CoI}^*}(0)e^{-(\frac{1}{\tau_{1,em}}+k_{1,nr}+k'_1)t},\\ n_{\mathrm{CoII}^*}(t) &= \frac{k'_1 n_{\mathrm{CoI}^*}(0)}{\left(\frac{1}{\tau_{1,em}} + k_{1,nr} + k'_1\right) - \left(\frac{1}{\tau_{2,em}} + k_{2,nr}\right)}\\ &\quad\times\left[e^{-(\frac{1}{\tau_{2,em}}+k_{2,nr})t} - e^{-(\frac{1}{\tau_{1,em}}+k_{1,nr}+k'_1)t}\right].\end{aligned} \tag{5}$$

Thus we obtain

$$\begin{aligned}&(a)\quad k_1 = \left(\frac{1}{\tau_{1,em}} + k_{1,nr} + k'_1\right)'\\ &(b)\quad k_2 = \left(\frac{1}{\tau_{2,em}} + k_{2,nr}\right).\end{aligned} \tag{6}$$

The respective experimental values are presented in Table II and are discussed later. To separate in 6(a) the rate constant k'_1 from the $(\frac{1}{\tau_{1,em}} + k_{1,nr})$ term, we carried out an additional experiment. We measured the $(\frac{1}{\tau_{1,em}} + k_{1,nr})$ value for a 7.3-nm planar Co nanolayer excited at 528.5, 376.5, and 286.9 nm. The emission was detected perpendicular to the nanolayer surface, with the resulting emission kinetics shown in Fig. 5.

In these measurements, the oscilloscope was triggered with a 5-ns delay. The decay kinetics were fitted using the relationship

$$I_{em}(t) = A_1 e^{-(\frac{t}{\tau_{las}})^2} + A_2 e^{-(\frac{1}{\tau_{1,em}}+k_{1,nr})t}, \tag{7}$$

where the first term describes the scattered excitation pulse and the second term describes the emission decay of the 7.3-nm Co nanolayer. The laser pulse duration τ_{las} is known quite well; therefore we adjusted only A_1, A_2, and $(\frac{1}{\tau_{1,em}} + k_{1,nr})$ parameters. Note that Fig. 5 also shows the fitting curves. Thus the fitted decay rate $(\frac{1}{\tau_{1,em}} + k_{1,nr})$ values were 16 ± 2, 19 ± 3, and $22 \pm 3\ \mu\mathrm{s}^{-1}$ for the respective excitation wavelengths. These values are in acceptable agreement with the k_2 values (see Table II), which describe the emission decay rate of the 11.3-nm Co nanolayer. Using these results, we calculated the values of the k'_1 rate constant, also listed in Table II.

TABLE II. Values of the k_1, k_2, and k'_1 rate constants for the emission growth and decay and the emission amplitude C. We fitted Eq. (3) to the data of Fig. 4.

Excitation wavelength (nm)	k_1 ($\mu\mathrm{s}^{-1}$)	k_2 ($\mu\mathrm{s}^{-1}$)	C (arbitrary units)	k'_1 ($\mu\mathrm{s}^{-1}$)
528.5	67 ± 5	17 ± 2	452	51 ± 7
376.5	81 ± 5	21 ± 3	752	62 ± 8
286.9	89 ± 6	26 ± 3	326	67 ± 9

D. Modeling analysis of the superemission

The referential used is illustrated in Fig. 1, with the z axis normal to the substrate; the model assumed the

TABLE III. Calculated energies for the experimentally observed absorbance transitions in the two nanolayers, cm^{-1} ($n \rightarrow n'$ transitions).

	$a = 7.3$ nm			$a = 11.3$ nm		
Band number	Energy	n	n'	Energy	n	n'
1	18922[a]	8	11	12413	9	12
2	26557[a]	8	12	16209	9	13
3	34857[a]	8	13	20283[b]	9	14
4	43820	8	14	24633	9	15
5				29260[b]	9	16
6				34165	9	17
7				39347[b]	9	18
8				44805	9	19
9				50541	9	20

[a]The bands excited by the dye laser.
[b]The bands excited by energy transfer from the 7.3-nm film.

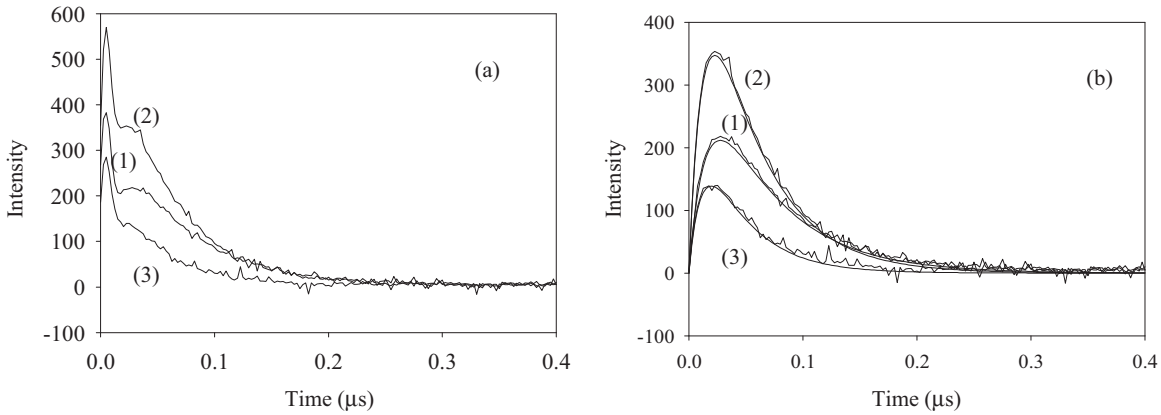

FIG. 4. Time evolution of the emission bands centered at 13 522, 21 946, and 31 478 cm^{-1}. The excitation wavelengths are the same as in Fig. 3: (1) 528.5 nm, (2) 376.5 nm, and (3) 286.9 nm. (a) Original data and (b) data after subtracting the scattered excitation laser pulse.

existence of a common continuum spectrum of states quantized in the horizontal plane (defined by the x and y axes) for the entire sample. This continuum spectrum only weakly interacts with the discrete spectra of the 7.3-nm nanolayer and the 11.3-nm track, quantized along the z direction. The energies of the electronic transitions between the electronic states of such nanostructures are described by the relationship (1), with the calculated values listed in Table III.

Comparing the absorption and the emission bands, we conclude that the emission transition occurs into an excited state; therefore we conclude that superemission takes place. In the emission spectra (2) and (3), we additionally observe lower-energy transitions with significantly lower intensities as compared to the main emission band (Fig. 3 and Table I), apparently resulting from the subsequent relaxation of the initially populated state.

The presently discussed energy transfer between the 7.3-nm nanolayer and the 11.3-nm nanotrack might occur by both exchange and dipole-dipole mechanisms [21,22]. The rate constant of the energy transfer may be described by the golden

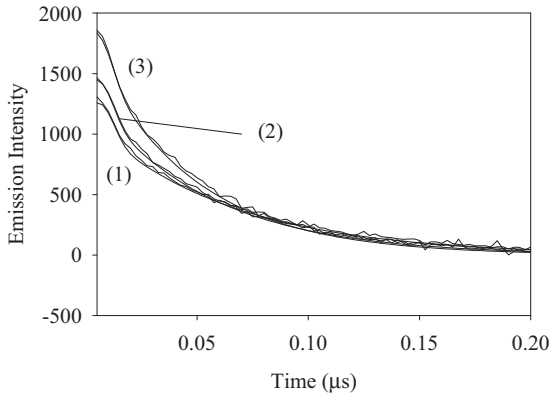

FIG. 5. Emission kinetics of the 7.3-nm planar Co nanolayer excited at (1) 528.5 nm, (2) 376.5 nm, and (3) 286.9 nm.

Fermi rule [23,24], presented as follows:

$$k_{DA} = \frac{2\pi}{\hbar}[|V_{DA,Exch}|^2 + |V_{DA,dd}|^2]\int_0^\infty \delta(E_D - E_A)dE_A$$
$$= \frac{2\pi}{\hbar}[|V_{DA,Exch}|^2 + |V_{DA,dd}|^2]\rho_A(E_D), \quad (8)$$

where the D and A subscripts refer to the energy donor (7.3-nm nanolayer) and the energy acceptor (11.3-nm nanotrack), and $V_{DA,Exch}$ and $V_{DA,dd}$ are the matrix elements of exchange and dipole-dipole interactions coupling the initial state

$$\Psi_{DA,1} = \psi_D^{\text{exc}}\psi_A^{\text{ground}} = \frac{4}{\sqrt{a_1 a_2}}\sin\left(\frac{\pi(n_1+m_1)}{a_1}z_1\right)\sin\left(\frac{\pi(n_2)}{a_2}z_2\right) \quad (9)$$

to the final state

$$\Psi_{DA,2} = \psi_D^{\text{ground}}\psi_A^{\text{exc}}\frac{4}{\sqrt{a_1 a_2}}\sin\left(\frac{\pi(n_1)}{a_1}z_1\right) \times \sin\left(\frac{\pi(n_2+m_2)}{a_2}z_2\right), \quad (10)$$

where superscripts *ground* and *exc* refer to the ground and excited electronic states, respectively, $\rho_A(E_D)$ is the active mode state density in the excited acceptor at the energy level E_D of the excited donor; $n_1 = 8$, $m_1 = 3,4,5$, $a_1 = 7.3$ nm, $n_2 = 9, m_2 = 5,7,9, a_2 = 11.3$ nm. We analyzed three coupling schemes: $m_1 = 3$ to $m_2 = 5$, $m_1 = 4$ to $m_2 = 7$, and $m_1 = 5$ to $m_2 = 9$. We took into account single-electron excited states both in the donor and the acceptor, using the two-electron exchange interaction in our analysis,

$$\hat{V}_{DA,Exch} = \frac{1}{4\pi\varepsilon\varepsilon_0}\frac{e^2}{|\vec{r}_1 - \vec{r}_2|} = \frac{1}{4\pi\varepsilon\varepsilon_0}\frac{e^2}{|z_1 - z_2|}, \quad (11)$$

where $\boldsymbol{r}_1$ and $\boldsymbol{r}_2$ are radius vectors defining positions of the two electrons in space, in the referential defined in Fig. 1. The dipole-dipole interaction is given by the Förster formula:

$$\hat{V}_{DA,dd} = \frac{1}{4\pi\varepsilon\varepsilon_0}\frac{e^2}{r^3}\left[(\vec{r}_D\cdot\vec{r}_A) - \frac{3}{r^2}(\vec{r}_D\cdot\vec{r})(\vec{r}_A\cdot\vec{r})\right], \quad (12)$$

TABLE IV. The calculated values of the matrix elements, the energy-transfer rate, and the effective state density $\rho_A(E_D)$.

Transitions	$R\,(10^{-6}\,\mathrm{cm}^{-2})$	$\rho_A(E_D)(1/\mathrm{cm}^{-1})$	$\tau_{2,em}k_{2,nr}$
$m_1 = 3 \rightarrow m_2 = 5$	3.7	459	0.37
$m_1 = 4 \rightarrow m_2 = 7$	4.1	503	0.72
$m_1 = 5 \rightarrow m_2 = 9$	5.8	384	1.56

where $\boldsymbol{r}$ is the distance between the oscillator centers, and $\boldsymbol{r}_D$ and $\boldsymbol{r}_A$ the distances between the centers of the oscillators and the respective optical electrons in D and A. The latter relationship may be rewritten as

$$\hat{V}_{DA,dd} = \frac{1}{4\pi\varepsilon\varepsilon_0}\frac{e^2}{r^3}(\vec{r}_D \cdot \vec{r}_A)[1 - 3\cos^2(\theta)], \qquad (13)$$

where θ is the angle between the z axis and the $\boldsymbol{r}$ vector direction. Averaging over the angles, we obtain

$$\hat{V}_{DA,dd} = -\frac{1}{4\pi^2\varepsilon\varepsilon_0}\frac{e^2}{r^3}(z_1 \cdot z_2). \qquad (14)$$

We calculated the value of the matrix element

$$R = \frac{2\pi}{\hbar}[|V_{DA,Exch}|^2 + |V_{DA,dd}|^2] \qquad (15)$$

using a homemade FORTRAN code, with the results of these calculations listed in Table IV.

Taking into account the value of $k'_1 = k_{DA}$ (Table II), Eq. (7), and the R values, we estimated the values of the effective state density $\rho_A(E_D) = (k'_1/R)$, also listed in Table IV. We believe that the high effective state densities in the acceptor result from the interactions of the discrete states with the continuum of the electronic states generated in the xy plane of the assembly. Presently we are not analyzing these interactions, leaving this task for the future *ab initio* calculations.

Taking into account the data of Table II, the emission quantum yields of 0.73 (1), 0.58 (2), and 0.39 (3), and the relationship

$$k_2 = \left(\frac{1}{\tau_{2,em}} + k_{2,nr}\right), \qquad (16)$$

we estimated the $\tau_{2,em}k_{2,nr}$ parameter defining the intensity distribution between the bands (see Table IV). Assuming as a rough approximation that the emission lifetime is independent of the excited state (m_2), we conclude that the radiationless relaxation rate constant increases by a factor of 4 as m_2 grows from 5 to 9. A very similar behavior is in fact observed experimentally, as the lower-energy emission bands are progressively weaker than the principal band (Table I and Fig. 3).

These results are quite notable with regard to the energy transfer from the excited state of the 7.3-nm Co nanolayer with a macroscopic surface area to the 11.3-nm Co nanotrack. Here the nanotrack works as an energy trap, with a larger state density and lower-energy excited states. Apparently we observe quasiresonant energy transfer, as presented in Fig. 6.

An external excitation source induces $n = 8 \rightarrow n = 11$ transition in the 7.3-nm Co nanolayer (Fig. 5, the potential box at the right). The energy of the latter transition is in quasiresonance with that of the $n = 9 \rightarrow n = 14$ transition of the 11.3-nm Co nanotrack. The energy transfer in these conditions operates at high efficiency, by the mechanism we already discussed. We expect that the excitation is distributed homogeneously over the nanotrack, with the population inversion created with respect to the $n = 10$ level causing superemission along the nanotrack surface towards both of its ends. Similar results are frequently obtained for the active optical media used in laser technology [25]. Note that no superemission was observed for the $n = 9 \leftarrow n = 11$ transition of the 7.3-nm Co nanolayer. This is probably caused by a fast energy transfer to the nanotrack. However, superemission was observed earlier [17] for a homogeneous Cr nanolayer, with excitation by a laser beam focused into a narrow line. The superemission in this case was observed along the thin pumped rectangle, with the emission times much shorter than the energy-transfer rates along the Cr layer.

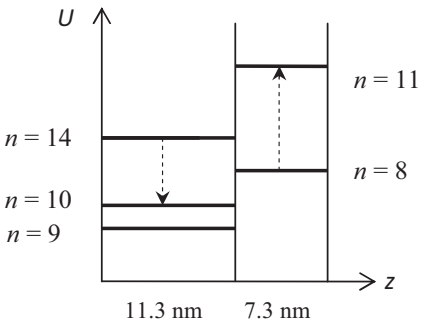

FIG. 6. Energy diagram of the superemission generated in the nanostructured Co device.

IV. CONCLUSIONS

We reported that a structured Co nanolayer can work as a light energy concentrator. We found that the concentrated emission quantum yield is dependent on the excitation energy, decreasing for higher photon energies: 0.73 at 528.5 nm, 0.58 at 376.5 nm, 0.39 at 286.9 nm. We analyzed the values of the $\tau_{2,em}k_{2,nr}$ parameter, concluding that the radiationless decay rate constant of the nanotrack states increases with the excitation energy. We developed a simple model for the energy transfer from the thinner nanolayer (7.3 nm) to the thicker nanotrack (11.3 nm), describing the experimental results with acceptable accuracy. We conclude that similar devices on a larger scale may be used for solar energy harvesting.

ACKNOWLEDGMENTS

The authors are grateful for the PR NASA EPSCoR grant No. NNX13AB22A for V.I.M. Both authors designed the experiments and analyzed the data. V.I.M. performed the experiments, and V.I.M. and I.K. designed and analyzed the theoretical models. The manuscript was prepared by V.I.M. and I.K.

[1] M. T. Allen, J. Martin, and A. Yacoby, Nat. Commun. **3**, 934 (2012).
[2] J. D. Joannopoulus, R. D. Meade, and J. N. Winn, *Photonic Crystals, Molding the Flow of Light,* 2nd ed. (Princeton University Press, Princeton, NJ, 1995).
[3] A. V. Zayats, J. Opt. A: Pure Appl. Opt. **5**, S16 (2003).
[4] F. R. Oulton, V. J. Sorger, T. Zentgraf, R. M. Ma, C. Gladden, L. Dai, G. Bartal, and Z. Zhang, Nature (London) **461**, 629 (2009).
[5] I. Khmelinskii and V. Makarov, Mater. Res. Bull. **72**, 50 (2015).
[6] V. Makarov and I. Khmelinskii, Mater. Res. Bull. **64**, 156 (2015).
[7] V. Makarov and I. Khmelinskii, J. Phys. Chem. Solids **75**, 670 (2014).
[8] V. Makarov, and I. Khmelinskii, Mater. Res. Bull. **50**, 514 (2014).
[9] V. Makarov and I. Khmelinskii, J. Appl. Phys. **113**, 084304 (2013).
[10] V. Makarov and I. Khmelinskii, J. Chem. Phys. **138**, 074705 (2013).
[11] V. Makarov, I. Khmelinskii, and S. Kochubei, J. Appl. Phys. **112**, 084310 (2012).
[12] V. Makarov, S. Kochubei, and I. Khmelinskii, J. Appl. Phys. **110**, 063717 (2011).
[13] V. Makarov and I. Khmelinskii, J. Phys. Chem. Solids **107**, 140 (2017).
[14] R. F. Oulton, V. J. Sorger, D. A. Genov, and D. F. P. Pile. Zhang, Nat. Photon. **2**, 496 (2008).
[15] S. A. Maier, P. G. Kik, H. A. Atwater, S. Meltzer, E. Harel, B. E. Koel, and A. A. G. Requicha, Nat. Mater. **2**, 229 (2003).
[16] A. D. Bernardo, O. Millo, M. Barbone, H. Alpern, Y. Kalcheim, U. Sassi, A. K. Ott, D. De Fazio, D. Yoon, M. Amado, A. C. Ferrari, J. Linder, and J. W. A. Robinson, Nat. Commun. **8**, 14024 (2016).
[17] I. Khmelinskii and V. Makarov, J. Mater. Res. Bull. **80**, 88 (2016).
[18] I. Khmelinskii and V. Makarov, Phot. Nano. Fund. Appl. **21**, 67 (2016).
[19] I. Khmelinskii and V. Makarov, J. Quant. Spectrosc. Radiat. Transfer **175**, 68 (2016).
[20] I. Khmelinskii and V. Makarov, Phot. Nano. Fund. Appl. **19**, 39 (2016).
[21] J. M. G. Martinho and J. C. Conte, Can. J. Chem. **61**, 1693 (1983).
[22] M. D. Dave and U. C. Pande, IOSR J. Appl. Chem. **3**, 11 (2012).
[23] B. H. Bransden and C. J. Joachain, *Quantum Mechanics*, 2nd ed. (Prentice Hall, Englewood Cliffs, NJ, 1999), p. 443.
[24] P. J. Robinson and K. A. Holbrook, *Unimolecular Reactions* (Wiley Interscience, Hoboken, NJ, 1972).
[25] W. Silfvast, *Laser Fundamentals* (Cambridge University Press, Cambridge, UK, 1996).